# Carbon oxidation in turbulent premixed jet flames: A comparative experimental and numerical study of ethylene, *n*-heptane, and toluene

Daniel I. Pineda [a,*], Laurel Paxton [b], Nikolaos Perakis [c,d], Chuyu Wei [a], Steven Luna [b], Hiba Kahouli [b], Matthias Ihme [c], Fokion N. Egolfopoulos [b], R. Mitchell Spearrin [a]

[a] *Department of Mechanical and Aerospace Engineering, University of California, Los Angeles, Los Angeles, CA 90095, USA*
[b] *Department of Aerospace and Mechanical Engineering, University of Southern California, Los Angeles, CA 90089, USA*
[c] *Department of Mechanical Engineering, Stanford University, Stanford, CA 94305, USA*
[d] *Chair of Space Propulsion, Technical University of Munich, Garching 85748, Germany*

## ARTICLE INFO

## ABSTRACT

An experimental and numerical investigation of the thermochemical structure of piloted premixed jet flames was conducted, encompassing laser absorption tomography measurements and large-eddy simulations (LES). The investigation was performed holding laminar flame speed, jet Reynolds number, and surrounding flow conditions constant while considering three different fuel types, namely an alkene, a normal alkane, and an aromatic fuel. Quantitative spatially-resolved thermochemical profiles of carbon monoxide (CO), carbon dioxide ($CO_2$), and temperature obtained from laser absorption tomography were compared against profiles predicted by the simulations for premixed ethylene-, toluene-, and *n*-heptane-air flames. Variations in flow structure are observed for the different fuels, highlighting fuel-specific chemical effects on the spatial evolution of the flames. Quantitative agreement of laser absorption tomography and LES results is generally observed for all flames, with larger deviations observed in the nozzle-near region for the higher molecular-weight fuels, indicating potential deficiencies in the turbulent mixing models. To the authors' knowledge, these measurements represent the largest molecular-weight fuels for which quantitative thermochemical data have been reported in a canonical piloted premixed jet-flame configuration. The spatially-resolved experimental measurements of CO, $CO_2$, and gas temperature provide valuable data which can be used as validation targets for the development of turbulent combustion models.

## 1. Introduction

Turbulent combustion has been the focus of extensive research efforts over the last several decades, with particular attention devoted to the investigation of hydrogen and light hydrocarbon fuels such as methane [1,2]. Although these studies provide valuable knowledge about highly turbulent flames in the thin and broken reaction zone regimes, relatively few investigations have assessed the importance of finite-rate chemistry in the context of fuel specific effects, particularly those caused by the variety of functional groups encountered in practical fuels. Considering that many energy conversion devices rely on turbulent combustion of liquid fuels comprising numerous high molecular weight components, the investigation of fuel effects is of particular importance.

Unlike lighter fuels, heavy hydrocarbons are susceptible to thermal decomposition in regions of the flame that precede oxidation [3–6]. In particular, at high-turbulence intensities, small-scale eddies penetrate these regions and modify its thermal and chemical structure [1,7,8]. Therefore, for heavy liquid fuels, the local flame structure could exhibit substantially different extinction and propagation behaviors compared to small-hydrocarbon fuels which are resistant to decomposition [9]. These phenomena especially depend on the mixture of smaller molecular fragments created from heavy fuel pyrolysis, which are eventually transported to the reaction zone [10]. Additionally, the diffusivities of heavy fuels and the products of their decomposition are substantially different than those of lighter fuels. Experimental investigations provide evidence that preferential diffusion effects—which could be enhanced for heavy-hydrocarbon fuels—affect the local flame structure and its overall response to hydrodynamics [9,11,12].

Recent developments in canonical burner designs, namely, the Hi-Pilot configuration developed by Driscoll and coworkers [13] and the Piloted Premixed Jet Burner (PPJB) developed by
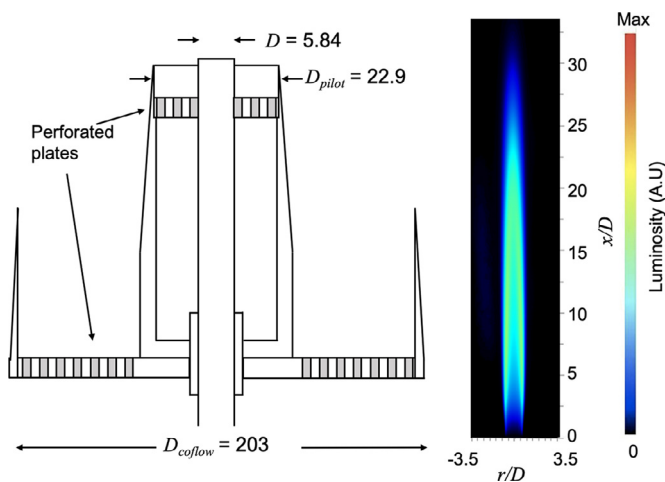
**Fig. 1.** Cross-section of the piloted premixed jet burner (PPJB) used for this study along with a chemiluminesence image of a representative flame depicting the radial and axial axes. All measurements are in mm [18].

Dunn et al. [14,15] have allowed the study of premixed jet flames in high Reynolds ($Re$) and Karlovitz ($Ka$) regimes of turbulence. Investigations with a similar PPJB at USC [16–18], shown in Fig. 1, have examined highly turbulent lean and near-stoichiometric premixed jet flames to explore fuel effects within the thin and broken reaction zones. Carbone et al. [16] captured time-averaged and instantaneous CH* chemiluminescence as well as the behavior of the mean and fluctuating velocity components for a wide range of $C_1$–$C_8$ jet flames at $Re$ of 12,500 and 25,000. The authors observed qualitative and quantitative deviation between flames of methane and other liquid fuels, and explored the potential of scaling parameters such as the laminar flame speed ($S_L$) and the adiabatic flame temperature ($T_{ad}$) to scale the flame observables. Only $S_L$ showed reasonable success in scaling the flame heights derived from CH* chemiluminescence. Paxton et al. [19] used the PPJB with an ignited coflow to study the effects of heat loss on flames in the broken reaction zones regime at $Re$ up to 50,000. Although the flame heights were shown to scale reasonably well with $S_L$, the differences between various fuels were not entirely suppressed in the broken reaction zones regime, where heat loss has been found to significantly affect the jet reactivity. These differences become more prominent at higher $Re$ and less pronounced for stronger burning flames.

Evidently, accurate and sufficiently resolved experimental measurements of thermochemical properties in reacting flows help distinguish physical behaviors of different fuels allowing for comparison with high-fidelity models, particularly for high $Re$ and $Ka$ number flames in the thin and broken reaction zones regimes. As such, several non-intrusive optically-based measurement techniques have been utilized to study turbulent flames. These include Rayleigh scattering [14,20–22], Raman scattering [14,23,24], laser-induced fluorescence (LIF) [25,26] and chemiluminescence [16,18]. With the exception of Raman scattering, these spectroscopic methods are generally not well-suited for quantitative species detection without extensive calibration [27]. Moreover, relatively weak Raman interactions pose practical difficulties due to the size and power of the required light sources. In contrast, laser absorption spectroscopy (LAS) provides for a calibration-free quantitative method to discern gas properties using compact low-power light sources [28]. Though traditionally limited in non-uniform flows due to the line-of-sight nature of the technique, the integration of tomographic methods has expanded applicability [29]. Recently, laser absorption tomography (LAT) was demonstrated to provide two-dimensional temperature and mole fraction measurements of

CO and $CO_2$ in turbulent premixed jet flames using mid-infrared semi-conductor lasers [30]. This method—employed in the present work—is suitable for small diameter ( ~ 1 cm) axially-symmetric reacting flows and utilizes tomographic reconstruction techniques [31,32] to extract time-averaged radial thermochemical profiles from spatially-resolved line-of-sight absorption measurements.

In this study, the thermochemical structure of turbulent jet flames of ethylene, *n*-heptane, and toluene, was experimentally and computationally examined using a piloted premixed jet flame burner. In this work, we define thermochemical structure as the spatially-resolved temperature and species concentration scalar fields in the reacting flow. The canonical piloted premixed jet flame burner configuration is widely used for turbulent combustion model validation [18,24,25,33–35]; this represents an opportunity for comparing quantitative LAT measurements with numerical models, specifically large-eddy simulations (LES). The measurements in this study provide spatially-resolved profiles of CO, $CO_2$, and temperature, targeting regions of carbon oxidation. These carbon oxides are chosen for their roles as critical combustion intermediates and products and their relevance in determining a boundary of heat release associated with the kinetically slow oxidation of CO to $CO_2$. The novel experimental dataset is accompanied by a series of LES using finite-rate chemistry models to examine the predictive accuracy of current models in capturing fuel effects in these flames, as well as to quantify the influence of turbulent flow-field behavior on the measurements.

The remainder of the manuscript has the following structure: The burner configuration, operating conditions, experimental techniques and simulations methods are presented in Section 2. The results and comparisons between experiments and simulations are discussed in Section 3, followed by a detailed uncertainty analysis of the experimental measurements in Section 4. The manuscript concludes with a summary of the major findings.

## 2. Experimental setup and methods

### 2.1. Piloted premixed jet burner (PPJB)

For this study, a modified PPJB burner [14] was utilized; the design, dimensions, and fuel delivery system of the burner are described in detail in previous studies [16,18,19]. The burner consists of a central jet tube with a diameter of $D = 5.84$ mm and a pilot and outer co-flow to stabilize the high-velocity central jet. A schematic of the burner configuration is shown in Fig. 1 along with a flame image depicting the axial ($x$) and radial ($r$) direction. Experiments were performed at a single jet Reynolds number, $Re_{jet} \equiv U_{jet}D/\nu = 50{,}000$, where $U_{jet}$ is the bulk flow velocity and $\nu$ is the kinematic viscosity at the burner exit. The jet flames were ethylene ($C_2H_4$)-air, *n*-heptane (*n*-$C_7H_{16}$)-air, and toluene ($C_6H_5CH_3$)-air mixtures at lean fuel-air molar equivalence ratios corresponding to $S_L = 20$ cm/s. $S_L$ is held constant to keep the burning rates and laminar flame properties (such as flame thickness) similar amongst the flames investigated [16]. All flows had an unburned mixture temperature of 298 K.

The pilot flame is a premixed $C_2H_4$-air flame with a temperature of 1780 K. The coflow surrounds the pilot and jet flames and is used to thermally insulate the jet. The coflow uses a premixed hydrogen-air flame at a global equivalence ratio of $\phi = 0.51$ to provide a temperature of $T_{coflow} = 1500$ K. This co-flow mixture is used to provide boundary conditions largely free of carbon atoms to minimize interference for the LAT technique probing the central jet flame [30]. The coflow and pilot flows have an unburnt velocity of 0.75 m/s, and these conditions are constant across all of the flames investigated in this study. The flame is assumed axisymmetric over the time interval (500 ms) in which

**Table 1**

Estimated key turbulence characteristics for the performed experiments. All values were calculated based on the kinematic viscosity of the unburned mixture, but the turbulent properties of the flow $L_{int}$ and $u'$ were measured in the shear layer at $x/D=15$.

| Fuel | $\phi$ | $U_{jet}$ (m/s) | $Re_{jet}$ | $S_L$ (cm/s) | $\frac{u'}{S_L}$ | $\frac{L_{int}}{\delta_f}$ | $Ka$ | $Da = \frac{\tau_r}{\tau_f}$ | $Re_t$ | $T_{ad}$ (K) | $H_{fl}$ (mm) |
|---|---|---|---|---|---|---|---|---|---|---|---|
| $C_2H_4$ | 0.55 | 133 | 50,000 | 20 | 80 | 9.41 | 624 | 0.12 | 5483 | 1706 | 196 |
| $n\text{-}C_7H_{16}$ | 0.65 | 133 | 50,000 | 20 | 80 | 9.81 | 631 | 0.12 | 5483 | 1804 | 216 |
| $C_6H_5CH_3$ | 0.70 | 133 | 50,000 | 20 | 80 | 9.46 | 669 | 0.11 | 5483 | 1931 | 230 |

LAT measurements (described in Section 2.2) are taken, averaged, and reported in this study.

Table 1 provides a summary of the conditions investigated. $S_L$ as well as the laminar flame thickness ($\delta_f$), the flame time ($\tau_f$), and adiabatic flame temperature ($T_{ad}$) were calculated in PREMIX [36]. The flame height ($H_{fl}$) was calculated using time-averaged line-of-sight CH* chemiluminescence data. $H_{fl}$ is defined as the position along the centerline of the jet at which the CH* intensity drops to 25% of its maximum value [16]. In this work, we determine the turbulent Reynolds number as $Re_t \equiv u'L_{int}/\nu$, where $u'$ is the turbulent intensity measured previously from PIV data in the shear layer at at $x/D = 15$ [19] and $\nu$ is the kinematic viscosity of the unburned reactants. The integral length scale ($L_{int}$) was calculated in the shear layer at $x/D = 15$ using the two-point correlations described by Carbone et al. [16] such that $L_{int} \approx 5.6$ mm [14]. It should be noted that $u'$ does not depend on $\phi$ while $L_{int}$ shows a minor dependence on $\phi$ and fuel type [16,18]. The Karlovitz number ($Ka$) is defined as $Ka \equiv \tau_f/\tau_\eta$, where $\tau_\eta$ is the Kolomogorov time scale determined as in previous studies [16,18]. As characterized by the high $u'$ and $Ka$, these flames are expected to fall near the boundaries of both the thin and broken reaction zone regimes.

## 2.2. Laser absorption tomography

Laser absorption tomography is a spatially-resolved diagnostic technique based on inversion of species-specific absorption projected along a multitude of optical lines-of-sight. LAT is thoroughly detailed in the literature and prior work [29,30,37–45], but we provide a brief overview here for context and nomenclature. For a non-uniform gas medium axially-symmetric in $r$ [cm], the Beer-Lambert law integrated over wavenumber $\nu$ [cm$^{-1}$]—or the projected absorbance area $A_{j,proj}(r)$ [cm$^{-1}$]—can be expressed for each line-of-sight and related to thermodynamic gas properties as [41]:

$$A_{j,proj}(r) = \int_{-\infty}^{\infty} -\ln\left(\frac{I_t}{I_0}\right)_\nu d\nu = \int_{-\infty}^{\infty} \alpha_\nu d\nu = \int_0^{L(r)} K_j(r)dl \qquad (1)$$

where $\alpha_\nu$ is the spectral absorbance, $I_0$ is incident intensity, and $I_t$ is transmitted intensity. $L(r)$ [cm] is the aggregate path length at radial position $r$. Integrating specific transitions in the spectral domain eliminates dependence on line-shape and composition, enabling calibration-free measurement of species concentration and temperature [28]. The thermochemical properties of interest are embedded in the radially-resolved absorption coefficient $K_j(r)$ [cm$^{-2}$] [30],

$$K_j(r) = P S_j(T(r)) X_{abs}(r) \qquad (2)$$

where the total pressure $P$ [atm] is assumed constant (1 atm), $S_j(T(r))$ [cm$^{-2}$/atm] is the linestrength of transition $j$ at temperature $T(r)$ [K], and $X_{abs}(r)$ is the mole fraction of the absorbing species. To obtain the radial distribution of $K_j(r)$ [cm$^{-2}$], a Tikhonov-regularized Abel inversion scheme [30–32] is implemented on $A_{j,proj}(r)$ measurements with regularization parameters determined by the L-curve method [46]. In this technique, Tikhonov regularization transforms the ill-conditioned set of equations generated by Abel transform into a well-conditioned set
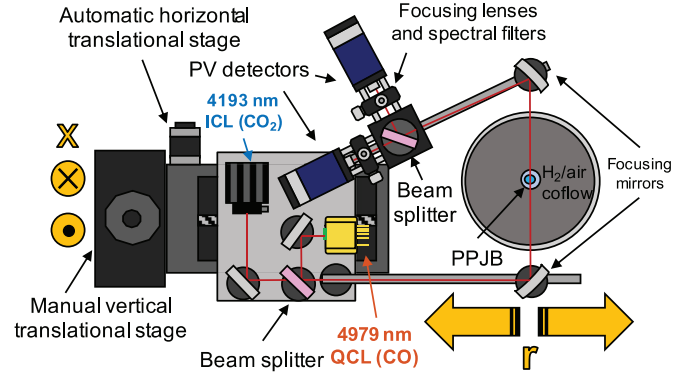


**Fig. 2.** Top-down schematic of PPJB facility with optomechanical translation stage system. The central jet is surrounded by a co-flow $H_2$/air flame. The lasers, optics, and detectors are mounted and move together while the burner remains stationary.

that is less susceptible to measurement errors as well as turbulent oscillations, promoting smooth reconstructed profiles that reflect the average flow field [32]. As demonstrated in previous work [30,43,45], this enables tomographic reconstruction of $K_j(r)$ in turbulent reacting flows which are approximately axisymmetric over the measurement time interval.

For multiple spectral transitions $j$, multiple $K_j(r)$ can be determined, and the ratio of two absorption coefficients reduces to a ratio of $S_j(r)$, which is a function of $T(r)$ only, as given by the following expressions:

$$R(r) = \frac{K_A(r)}{K_B(r)} = \frac{S_A(T(r))}{S_B(T(r))} = f(T(r)) , \qquad (3)$$

and $S_j(T)$ can be calculated using information readily available in spectral databases [47] (See Sec. 4). With this, the gas temperature $T(r)$ can be determined with the simultaneous measure of two transitions at any location $r$ [30,41]. Once temperature is known, mole fraction $X_{abs}(r)$ can be directly calculated from measured $K_j(r)$ of either transition through Eq. (2). In this study, we implement this strategy at multiple measurement planes of a turbulent jet flame to construct two-dimensional images of temperature and gas composition [30].

A scanned-wavelength direct-absorption method was employed with a tunable quantum cascade laser (QCL) and a tunable interband cascade laser (ICL) to spectrally resolve select ro-vibrational transitions in the fundamental vibrational bands of CO and $CO_2$ near 4.9 and 4.2 $\mu$m, respectively. The compact lasers and detectors were mounted to a 150 $\times$ 150 mm$^2$ optical breadboard fixed to a dual horizontal and vertical translation stage as shown in Fig. 2, to characterize the time-averaged thermochemical structure of the flame. The concentric laser beams were focused to beam diameters of ~ 0.5 mm. During the measurement, the optomechanical assembly translates horizontally via an automatic translation stage, and the encoder signals of its stepper motor are used to resolve the spatial location of the measurements in time. A manual vertical stage translates the entire assembly to repeat the measurements at different heights downstream of the jet exit. The lasers are current-modulated to scan in wavelength at 1 kHz, and the sig-

nals are temporally and spatially averaged [30] to yield an overall spatial resolution in the radial direction of 0.5 mm (the same as the beam diameter), while the resolution in the vertical direction was similar but sampled step-wise at 20 mm intervals. Notably, Eqs. (1)–(3) are strictly valid for steady flows—the effects of rapid turbulent flowfield fluctuations on Eq. (2) and subsequent thermochemical interpretation are discussed in more detail in Section 2.4. Since the thermochemical gradients in the flames are much lower in the vertical direction than the in the radial direction, a sparse vertical sampling and effective resolution was deemed acceptable for the purposes of this comparative study.

It is important to note that two ro-vibrational transitions must be sufficiently resolved for any given species to determine gas temperature and subsequently mole fraction. For each species, two ro-vibrational transitions $B(v'', J'')$, are targeted, where $B$ indicates the branch (R, P, or Q), while $v''$ and $J''$ indicate the lower-state vibration and rotation quantum numbers, respectively [48]. We target the P(0,31) and P(1,26) lines of CO and the R(0,58) line and R(1,105+106) doublet line of $CO_2$ [30]. Although the reconstructions of $K_j(r)$ are valid within their uncertainties for all $r$, regions of the flow with very low absorption coefficient (signal-to-noise ratio $< 5$) are less reliable for quantitative interpretation and are not plotted. For the targeted wavelengths in this study, this typically corresponds to regions of the flow that are either much below $\sim 1000$ K or with a mole fraction less than $\sim 5 \times 10^{-4}$. Further details regarding the measurement uncertainty are available in Section 4, while more information about the wavelength selection and temperature sensitivity is available in previous work [30].

### 2.3. Large-Eddy simulations

The measurements are complimented by large-eddy simulations. For this, a finite-rate combustion model using reduced chemical models is utilized for the simulation of all three fuels. The turbulent reacting flow field is described as solution to Favre-filtered conservation equations for mass, momentum, total energy, and species, taking the following form:

$$\partial_t \overline{\rho} + \nabla \cdot (\overline{\rho}\widetilde{\boldsymbol{u}}) = 0, \tag{4a}$$

$$\partial_t (\overline{\rho}\widetilde{\boldsymbol{u}}) + \nabla \cdot (\overline{\rho}\widetilde{\boldsymbol{u}}\widetilde{\boldsymbol{u}}) = -\nabla \overline{P} + \nabla \cdot \overline{\boldsymbol{\tau}}_{v+t}, \tag{4b}$$

$$\partial_t (\overline{\rho}\widetilde{e}) + \nabla \cdot (\overline{\rho}\widetilde{\boldsymbol{u}}\widetilde{e}) = -\nabla \cdot (\widetilde{\boldsymbol{u}}\overline{P}) + \nabla \cdot (\overline{\boldsymbol{\tau}}_v \cdot \widetilde{\boldsymbol{u}}) - \nabla \cdot \overline{\boldsymbol{q}}_{v+t}, \tag{4c}$$

$$\partial_t (\overline{\rho}\widetilde{Y}_k) + \nabla \cdot (\overline{\rho}\widetilde{\boldsymbol{u}}\widetilde{Y}_k) = -\nabla \cdot \overline{\boldsymbol{j}}_{k,v+t} + \overline{\dot{\omega}}_k, \tag{4d}$$

where $\rho$ is the density, $\boldsymbol{u}$ is the velocity vector, $P$ is the pressure, $e$ is the specific total energy, $\boldsymbol{\tau}$ is the stress tensor, $\boldsymbol{q}$ is the heat flux, and $Y_k$, $\boldsymbol{j}_k$, and $\dot{\omega}_k$ are the mass fraction, diffusion flux, and chemical source term for species $k$, and the species equations are solved for $k = 1, \ldots, N_S - 1$ where $N_S$ is the number of species. Subscripts $v$ and $t$ denote viscous and turbulent quantities, respectively.

For the subgrid-scale turbulence-chemistry interaction, the dynamic thickened-flame model [49] is employed, and the Vreman model [50] is used to represent the turbulent subgrid stresses. A sensitivity study was performed and a maximal thickening factor of 3 was found to be adequate for the current choice of mesh resolution while balancing available computational resources. The source term of CO is used as a sensor—the maximum net production rate of CO in a free flame simulation corresponding to each fuel is used as the activation threshold. A duplicate set of simulations for the $(C_6H_5CH_3)$-air jet flame was performed with the source term of OH used as a flame sensor, with no significant differences found in the final profiles. Therefore, CO, which is measured in the experiments, is used for all simulations presented in this study.

The equations for mass, momentum, energy, and species are discretized using a finite-volume formulation with a sensor-based hybrid scheme for the convective fluxes [51,52]. In this hybrid method, a high-order central scheme is combined with a second-order essentially non-oscillatory scheme. A second-order Strang-splitting scheme [53] is applied to separate the convection, diffusion, and reaction operators. A strong stability preserving 3rd-order Runge-Kutta (SSP-RK3) scheme [54] is used for time integration of non-stiff operators. The reaction chemistry is integrated using a semi-implicit Rosenbrock–Krylov scheme [55], which is 4th-order accurate in time and has linear cost with respect to the number of species.

All chemical kinetic mechanisms employed in these simulations are DRG-reduced [56] and validated against calculations [57] of 1D laminar flames with $S_L$, temperature profiles, and major species profiles as reduction targets. For $C_2H_4$, a DRG reduced model based on USC Mech II [58] was used. For both $n$-$C_7H_{16}$ and $C_6H_5CH_3$, reduced-order models are based on JetSurF 2.0 [59]. Due to solution stiffness, the $n$-$C_7H_{16}$ and $C_6H_5CH_3$ models were modified by removing several of the smallest timescale reactions. The performance of these reduced mechanisms with respect to species profiles in laminar flames, laminar flame speed, and ignition delay is described in further detail in Supplementary material A.

The size of the three-dimensional computational domain is 0.35 m $\times$ 0.26 m $\times$ $2\pi$ in the axial, radial, and azimuthal directions, respectively. The grid uses 401 non-uniformly distributed points in axial direction, concentrated in the vicinity of the injection plane to ensure sufficient resolution of the turbulent scales. The axial resolution directly after the injection plane results to first-cell size of 93 μm, while a growth ratio of 0.65% is chosen for the first 2 jet diameters downstream of the inlet. The radial direction is discretized with 125 points, clustered in the shear layers between the different streams, whereas 160 points are used for the circumferential resolution. At the inlet of the jet stream, a turbulent velocity profile is applied, with turbulent fluctuations prescribed to match the experimentally measured velocity field. For the co-flow and pilot streams, the velocity corresponding to the burnt products along with the adiabatic chemical equilibrium temperature and composition is prescribed.

The LES computations provide spatially-resolved instantaneous thermochemical properties (temperature, mole fractions, reaction rates) for the different flames under investigation. Representative instantaneous flow-fields for CO and $CO_2$ obtained from these simulations for the three different fuels are shown in Fig. 3. Although the CO and $CO_2$ concentrations near the pilot flame region are similar for all of the flames, fuel-specific effects are immediately notable from the instantaneous images; regions of the flows downstream of the pilot flame exhibit local CO and $CO_2$ mole fraction levels which are highest for the $(C_2H_4)$-air flame, next-highest for the $(n$-$C_7H_{16})$-air flame, and lowest for the $(C_6H_5CH_3)$-air flame. For adequate comparison with the experimental laser absorption tomography measurements—which represent time- and azimuthally-averaged thermochemistry—the simulations are run for five convective flow-through times and statistical flow-field results are obtained by averaging both in time and about the azimuthal direction. For each flame, a subset of time-resolved (subsampled at $\Delta t = 7$ μs) instantaneous thermochemical profiles along a single line of sight at various $x/D$ were used for quantifying the influence of correlated variable fluctuations on the LAT measurements, as described in the next subsection.

### 2.4. Comparison of time-averaged results

In this study, we compare time-averaged measurements of spatially-resolved thermochemistry based on laser absorption tomography with time- and azimuthally-averaged predictions
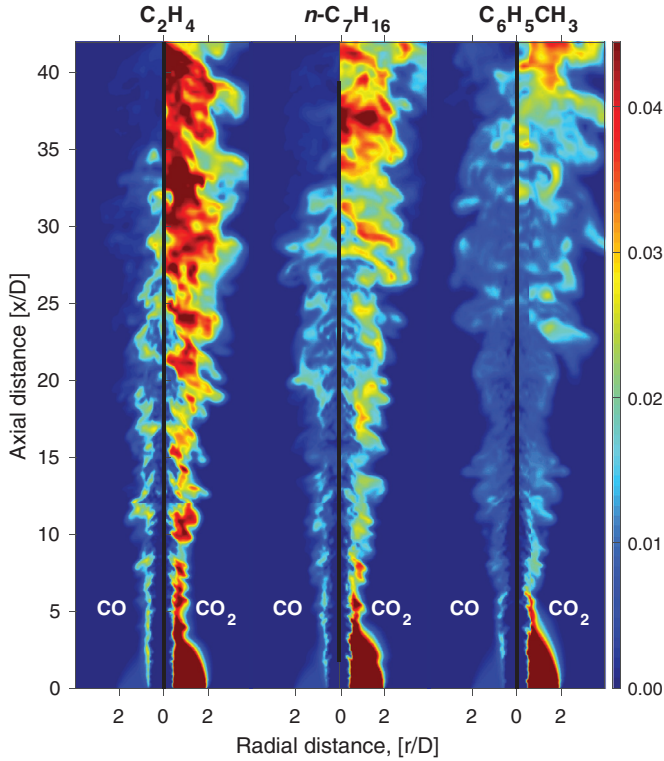
**Fig. 3.** Instantaneous (non-time-averaged) LES predictions of CO and $CO_2$ mole fraction for the flame conditions shown in Table 1.



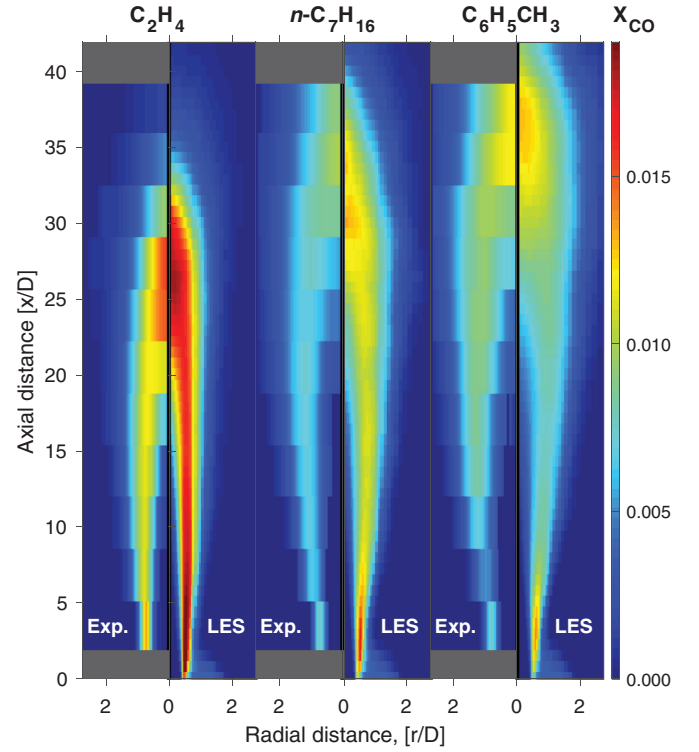**Fig. 4.** Two-dimensional CO mole fraction for each fuel from both experimental results (left sides) and LES predictions (right sides).

by large-eddy simulations. It is important to recognize that turbulence-induced thermochemical fluctuations in both the experiments and numerical simulations—resulting in correlated flowfield scalars [60]—can influence our ability to make direct comparisons of these averaged values. To demonstrate these influences, we decompose the instantaneous absorption coefficient $K_j$ in Eq. 2 into its mean and fluctuation, $\overline{K_j}$ and $K'_j$, respectively:

$$K_j = \overline{K_j} + K'_j = P\left(a\overline{T} + aT' + b\right)\left(\overline{X_{abs}} + X'_{abs}\right) \tag{5}$$

where temperature-dependent linestrength is expressed via a first-order Taylor expansion in linestrength $S_j(T) = aT + b$, and mole fraction $X$ and temperature $T$ are each decomposed into their mean ($\overline{X}$ and $\overline{T}$) and fluctuation ($X'$ and $T'$) values. Although linestrength $S_j(T)$ is usually nonlinear with respect to temperature [48], this simplified expression illustrates the influence of correlated flowfield scalars on the time-averaged measurement. Taking the mean of Eq. 5, and assuming that the mean of each fluctuation is zero, we obtain:

$$\overline{K_j} = PS_j(\overline{T})\overline{X_{abs}} + aP\overline{T'X'_{abs}} \tag{6}$$

Here, $a$ is the slope of the linestrength with respect to temperature at the averaged temperature, $\partial S_j(T)/\partial T|_{\overline{T}}$, which can be determined using information in spectral databases. In Eq. (6), $\overline{T'X'_{abs}}$ represents the time-averaged correlation between the turbulent fluctuations in temperature and mole fraction, which cannot a priori be assumed as zero. More generally, in turbulent flows for which $\overline{T'X'_{abs}}$ is considered sufficiently large,

$$\overline{K_j(T, X_{abs})} \neq K_j\left(\overline{T}, \overline{X_{abs}}\right) \tag{7}$$

In this work, we estimate the influence of correlated variables for a variety of axial locations in the flames by using $\overline{T'X'_{abs}}$ obtained from the LES simulations. Although our measurements of $\overline{K_j}$ are convoluted by these phenomena, we show in our uncertainty analysis presented in Sec. 4 that the anticipated measurement biases

by $\overline{T'X'_{abs}}$ in the targeted flows are within the calculated experimental uncertainties. Therefore, we simply quantify it as an independent uncertainty in $\overline{K_j}$ with which to consider when comparing the results of the experiments and simulations.

## 3. Results and discussion

### 3.1. Comparative two-dimensional thermochemistry

Experimental and numerical results from all planes are assembled into two-dimensional images of mole fraction for CO and $CO_2$ in Figs. 4 and 5 to distinguish and compare the thermochemical structure amongst the different fuels. Although the vertical resolution of the experimental measurements is much coarser (20 mm) than that of the radial resolution or the corresponding vertical resolution in the simulations, the data are presented as images for easier comparison. For the CO mole fraction images shown in Fig. 4, a hollow region in the core of the jet flame is apparent for all fuels studied, and this region is longer for the ($n$-$C_7H_{16}$)-air and ($C_6H_5CH_3$)-air jet flames. This indicates that $n$-$C_7H_{16}$ and $C_6H_5CH_3$ in their corresponding flames take longer to initiate carbon oxidation. These hollow regions appear larger in the measurements than in the LES predictions, especially in the ($n$-$C_7H_{16}$)-air flame. The measured and LES-predicted peak locations of CO are in good agreement throughout the flames, although less CO is observed in the experiments than predicted for the ($C_2H_4$)-air and ($n$-$C_7H_{16}$)-air flames. At the base of the jet flame near the pilot for all the fuels, there are high peak concentrations of CO in both the experimental observations and the LES predictions, followed by a decrease in peak concentration in the direction of flow and then a subsequent increase. Despite a consistent pilot reactant mixture for all flames, this peak CO concentration near the pilot is highest for the ($C_2H_4$)-air jet flame, followed by the ($n$-$C_7H_{16}$)-air and ($C_6H_5CH_3$)-air jet flames, reflecting fuel-specific effects early in the oxidation process.
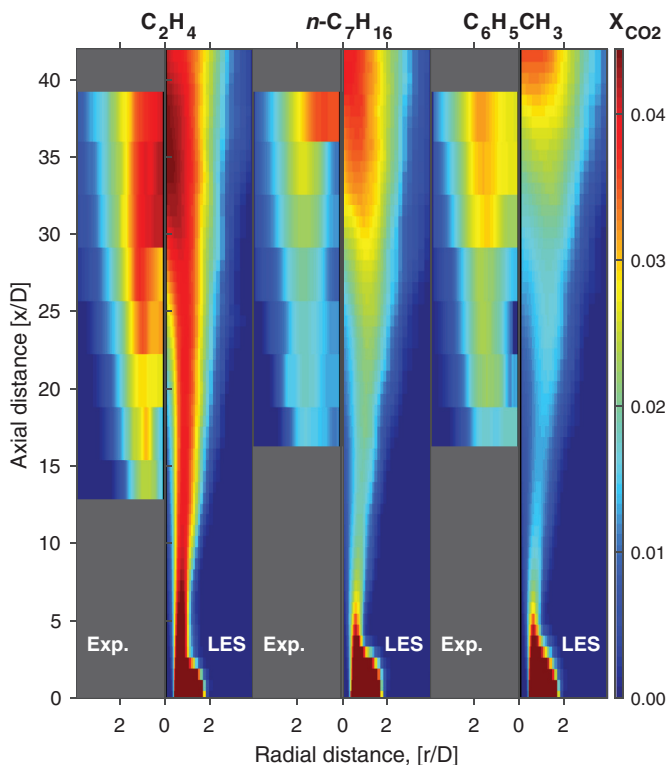
**Fig. 5.** Two-dimensional $CO_2$ mole fraction for each fuel from both experimental results (left sides) and LES predictions (right sides).



**Fig. 6.** Radial profiles of CO and $CO_2$ mole fraction obtained from LAT measurements alongside predicted results from simulations.

More information is gleaned from looking at the $CO_2$ mole fraction image in Fig. 5. We note that for the lowest vertical planes, the mole fraction of $CO_2$ is not experimentally resolvable in the flow due to weak absorbance in the R(1,105+106) doublet pair in these regions. $CO_2$ forms most appreciably near the core regions of the flames at locations of $x/D$ beyond which the mole fraction of CO has begun to decrease in the axial direction, consistent with continued carbon oxidation in the flame. The trends in experimental $CO_2$ mole fraction profiles amongst the fuels are well-captured by the LES predictions, with both $(n\text{-}C_7H_16)$-air and $(C_6H_5CH_3)$-air flames forming $CO_2$ most appreciably at larger $x/D$ than the $(C_2H_4)$-air flame. For the $(n\text{-}C_7H_{16})$-air flame, experimentally measured $CO_2$ mole fraction is observed to increase in the core of the flame suddenly in the highest $x/D$ plane measured, resembling the corresponding $CO_2$ image from the instantaneous LES predictions shown in Fig. 3, while the averaged LES predictions show a more gradual increase. Conversely, in the $(C_6H_5CH_3)$-air flame, the concentration of $CO_2$ in the core of the flame is generally underpredicted. Although the experimentally measured $CO_2$ mole fraction near the pilot is not available, the fuel ordering in peak $CO_2$ concentration predicted by LES follows the same trends as those of CO—the concentrations are highest for the $(C_2H_4)$-air jet flame, followed by the $(n\text{-}C_7H_{16})$-air and $(C_6H_5CH_3)$-air jet flames.

Although all tested fuels in their respective equivalence ratios have the same $S_L$, the thermochemical structures of the flames are distinguished from one another readily, highlighting the effects of fuel chemistry in turbulent jet flames. As with the instantaneous LES predictions shown in Fig. 3, the measurements and averaged LES predictions of the $(C_2H_4)$-air flame show the highest concentrations of both CO and $CO_2$, although the ordering is less immediately apparent with regards to the $(n\text{-}C_7H_{16})$-air flame and $(C_6H_5CH_3)$-air flame. As the conversion of CO to $CO_2$ is the final step of carbon oxidation, regions of the flow where CO vanishes can be interpreted as "boundaries" of the flame, allowing for com-
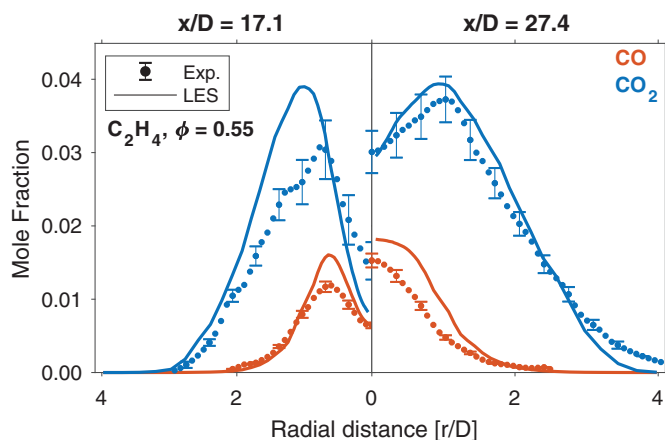
parison with the flame height, $H_{fl}$, measured by CH* chemiluminescence. Though not entirely captured in the domain considered in this study, the fuel-ordering for flame height as interpreted by the extent of the predicted and the measured CO concentration qualitatively agrees with the ordering of $H_{fl}$ in Table 1: The alkene $C_2H_4$ provides a shorter flame than the normal alkane $n\text{-}C_7H_{16}$, which is only slightly shorter than that provided by the aromatic $C_6H_5CH_3$. These results are also in agreement with previous investigations of fuel effects on $H_{fl}$ using the PPJB [18,19]. Notably, the $(n\text{-}C_7H_{16})$-air and $(C_6H_5CH_3)$-air jet flames also have wider flame brushes and a wider and taller core region without CO or $CO_2$, indicating slower overall oxidation and increased diffusion of fuel or fuel fragments in the flame.

### 3.2. Single plane analysis

To better characterize the agreements and disagreements between the LES predictions and experimental measurements while considering experimental uncertainties, radial profiles obtained for specific $x/D$ planes above the burner are examined in more detail. Details regarding the calculation of measurement uncertainties shown as error bars can be found in Section 4. Although plots of representative data are provided here (with some points omitted for plot readability), the reader is referred to Supplementary material B containing plots of experimental and numerical data in *all* $x/D$ planes to assist in comprehension of the analysis.

#### 3.2.1. $(C_2H_4)$-air jet flame

Representative radial profiles of mole fractions for CO and $CO_2$ are shown for two different heights above the jet exit for the ethylene-air jet flame in Fig. 6. For the lower plane shown of 100 mm $(x/D = 17.1)$, CO and $CO_2$ are concentrated at a radial distance within two jet diameters, with CO concentrated closer to $D$. Notably, there is a lower concentration of both CO and $CO_2$ in the core of the flame. For the higher plane measured at 160 mm $(x/D = 27.4)$, CO and $CO_2$ are more concentrated at the core of the flow, with peak CO mole fraction occurring at the centerline. $CO_2$ is formed toward larger $r/D$. For both planes, there is much more $CO_2$ than CO, indicating relatively fast oxidation of CO to $CO_2$ as it is formed. The averaged LES prediction captures the spatial extent of both species, despite nominally over-predicting peak concentrations in the lower plane.

Figure 7 shows representative radial profiles of temperatures determined from both CO (orange) and $CO_2$ (blue) laser absorption tomography measurements for the same planes of the same $(C_2H_4)$-air jet flame. The LAT temperature results from regions in
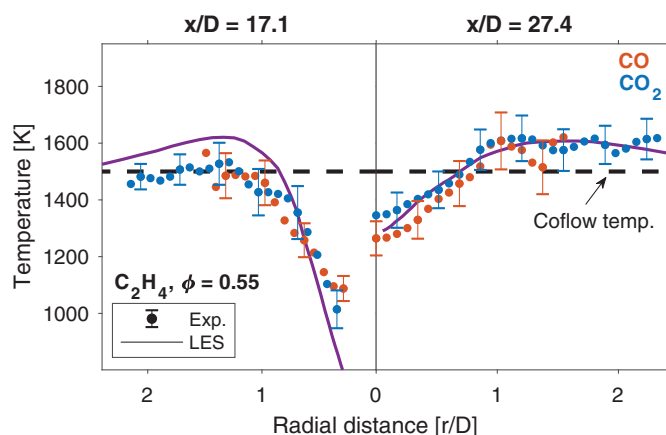
**Fig. 7.** Temperature profiles obtained from CO and $CO_2$ LAT measurements and corresponding simulation predictions. The co-flow temperature is indicated with a dashed black line.



**Fig. 8.** Radial profiles of CO and $CO_2$ mole fraction obtained from LAT measurements alongside predicted results from simulations.



**Fig. 9.** Radial profiles of CO and $CO_2$ mole fraction obtained from LAT measurements alongside predicted results from simulations.

which both CO and $CO_2$ are present in the flow generally show good agreement within experimental uncertainty, although regions of the flow with low species concentration have greater uncertainty due to lower spectral absorbance [30]. At the lower plane of 100 mm ($x/D = 17.1$), the temperature increases toward the co-flow temperature of 1500 K. The core of the flow has a much lower temperature, just above 1000 K. At the higher plane of 160 mm ($x/D = 27.4$), the measured temperature peaks near approximately the jet diameter ($r/D \approx 1$), although the average LES predicted temperature is nominally higher. The core of the flow has a higher temperature ($T \approx 1300$ K) than in the lower plane, which is still lower than the coflow temperature of 1500 K. The averaged LES model accurately predicts the radial temperature distribution within experimental uncertainty for both planes, although in the lower plane ($x/D = 17.1$) the simulation over-predicts the gas temperature. The averaged simulation results are consistent with the mole fraction results shown in Fig. 6, depicting an over-prediction of oxidation rate closer to the jet exit.

The underprediction of peak temperature and CO mole fraction begins in the lowest measured planes (See Supplementary material B), closest to the pilot—instead of a sharp region of high temperature around $r/D = 1$, the temperature gradient is more diffuse, with a higher than-predicted temperature in the core and a lower-than predicted temperature on the edges of the flame zone. This radially-smoothed evolution of the reaction zone—which persists through higher planes in the axial direction—suggests a higher degree of mixing of the flame zone with the hot coflow and the core jet than predicted, faster-than predicted oxidation in the pre-mixed jet core and slower-than-predicted oxidation in the reaction zone, or both. Beyond $x/D = 24.0$, the experimental and numerical results are in much better agreement, as seen in the right of Figs. 6 and 7.

### 3.2.2. (n-$C_7H_{16}$)-air jet flame

Representative radial profiles of CO and $CO_2$ mole fractions are shown for the n-heptane-air jet flame in Fig. 8. For the lower plane of 100 mm ($x/D = 17.1$), CO and $CO_2$ are concentrated largely within two jet diameters, as with the ($C_2H_4$)-air jet flame. In contrast, the overall concentrations (measured and predicted) of both species are much lower than in the ($C_2H_4$)-air jet flame for $x/D = 17.1$. The radial extent of both species is larger than predicted by the LES modeling, and the peak values are over-predicted. For the higher plane shown of 220 mm ($x/D = 37.7$), the averaged LES predictions are in much better agreement with experimental observations; the peak concentrations of CO and $CO_2$ agree within experi-
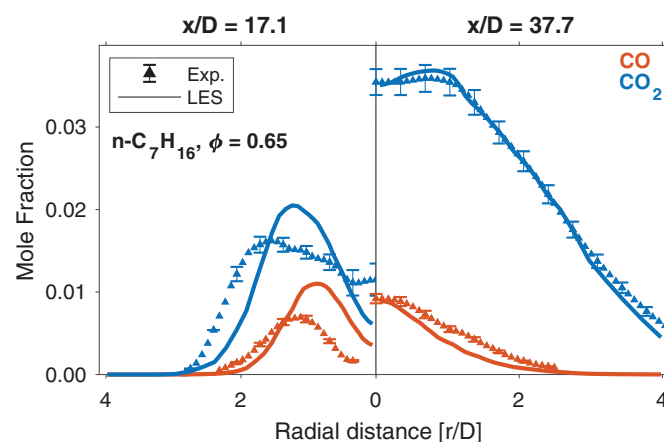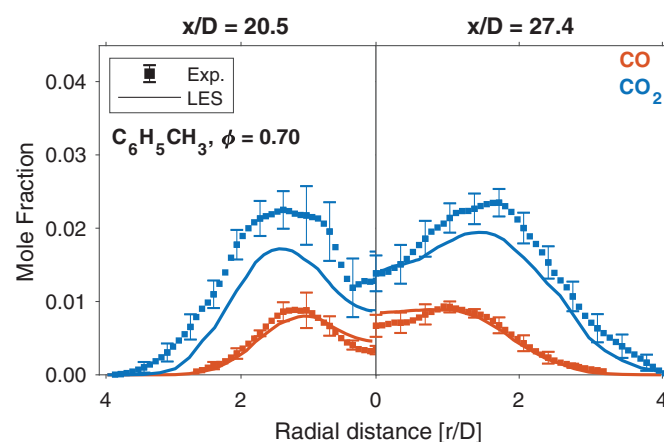
mental uncertainty, though a slight underprediction of CO concentration is noted at larger $r/D$.

As with the ($C_2H_4$)-air jet flame, the overprediction of temperature and CO mole fraction in the reaction zone begins in the lowest $x/D$ planes (Supplementary material B), in which both predicted and measured mole fractions are decreasing with $x/D$ as the products of the pilot flame mix with the hot co-flow. Although the predicted and observed radial extents of CO mole fraction are in good agreement for $x/D = 3.4$, the peak of CO concentration shifts to larger than predicted $r/D$ at $x/D = 6.8$, wherein the temperature of the reaction zone is also less than predicted. For $x/D > 10$, the model predictions of the radial temperature profiles are in excellent agreement with the experimental measurements, although the overprediction of CO mole fraction persists. The axial evolution of the flame between the two $x/D$ planes shown in Fig. 8 reveals increasing model disagreement in the core of the jet flame; beyond $x/D = 17.1$, both temperature and CO and $CO_2$ mole fraction are increasingly overpredicted in the core flow until $x/D = 37.7$. At larger $r/D$ for $x/D \geq 24.0$, the diffusion of species into the hot co-flow is well-captured by the LES predictions, and the predicted mole fractions of both CO and $CO_2$ are in excellent agreement with measured values.

### 3.2.3. ($C_6H_5CH_3$)-air jet flame

Representative radial profiles of CO and $CO_2$ mole fractions are shown for the toluene-air jet flame in Fig. 9. The toluene-air jet flame is generally observed to have a wider flame brush than the
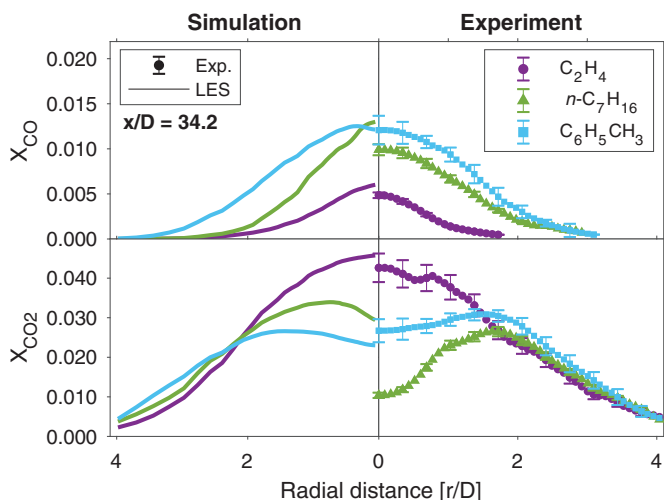
**Fig. 10.** Comparative computational (left) and experimental (right) radial profiles of CO and $CO_2$ mole fractions at $x/D = 34.2$.

other flames, indicated by the larger radial spread of both CO and $CO_2$. For the lower plane of 120 mm ($x/D = 20.5$) shown, CO and $CO_2$ mole fractions are lower in the core of the flame, and peak near approximately the jet diameter ($r/D \approx 1$). Experimental uncertainty for $CO_2$ mole fraction is larger in this core region, owing to significant variation in both $CO_2$ absorption coefficients $K_{R(0,58)}$ and $K_{R(1,105+106)}$ in the core of the flow at the lower planes for this jet flame. The averaged LES predictions for CO generally agree within experimental uncertainty in both planes shown, while $CO_2$ is underpredicted. For the higher plane of 160 mm ($x/D = 27.4$), the distribution of CO and $CO_2$ increases slightly to larger $r/D$, and the experimental uncertainties are smaller relative to those in the lower plane. Despite nominally underpredicting the $CO_2$ mole fraction, the averaged LES predictions capture the shapes of the profiles well.

As with both the ($C_2H_4$)- and ($n$-$C_7H_{16}$)-air flames, the overprediction of temperature and CO mole fraction in the reaction zone of the ($C_6H_5CH_3$)-air flame begins in the lowest $x/D$ planes (Supplementary material B), in which both predicted and measured CO and $CO_2$ mole fractions are decreasing with $x/D$ due to mixing of the pilot flow with the hot co-flow. As $x/D$ increases, the temperature rises in the core of the flame and the agreement between measurement and prediction is good, though as with the ($n$-$C_7H_{16}$)-air flame, the CO mole fraction in this same region is overpredicted until $x/D \geq 17.1$. Unlike the ($C_2H_4$)- and ($n$-$C_7H_{16}$)-air flames, peak $CO_2$ mole fraction in the reaction zone is consistently underpredicted by the LES until $x/D = 37.7$, although temperature in the core of the flow is in agreement for these planes. At $x/D = 37.7$, however, the temperature of the core flow, which is experimentally determined to be lower than the coflow temperature, is overpredicted by the LES.

### 3.2.4. Comparative single-plane analysis

Notable fuel-specific trends predicted by LES are observed in the experimental measurements. The top of Fig. 10 shows experimental and computational radial profiles of CO and $CO_2$ mole fraction at a significantly downstream location ($x/D = 34.2$). The averaged LES predictions of peak CO mole fraction are all nominally in agreement with the experimental measurements, with the exception of those of the ($n$-$C_7H_{16}$)–air flame. With that exception, the fuel ordering in peak CO and $CO_2$ concentration and behavior with increasing radial direction amongst the fuels are in agreement. The ($C_2H_4$)-air flame has the highest peak levels of CO of the fuels, and the steeper gradients in concentration indicate a thinner re-

action zone with more rapid oxidation than the other fuel-air mixtures in these conditions, which is observed in Figs. 4 and 5. The bottom of Fig. 10 shows a similar plot for $CO_2$ mole fraction. For $CO_2$ mole fraction, the averaged LES predictions and experimental measurements are in good agreement for both the ($C_2H_4$)-air and ($C_6H_5CH_3$)-air flames, both nominally and qualitatively. The results show more disagreement for the flame fueled by the alkane $n$-$C_7H_{16}$, though—specifically, the reaction zone of the ($n$-$C_7H_{16}$)-air flame is concentrated near $r/D = 2$ rather than closer to the centerline. Beyond $r/D = 2$, in the higher-mixing regions nearer to the hot co-flow, the fuel ordering in $CO_2$ concentration predicted by the LES is in excellent agreement with experimental observations. The disagreement in the flame core ends 20 mm downstream at $x/D = 37.7$, as seen previously in the right of Fig. 8 and in the middle of Fig. 5, reflecting a rapid advance in combustion progress in the core of the flame that is not captured by the LES predictions. Both results suggest that the $n$-$C_7H_{16}$ in the flame core is oxidizing at a lower rate than predicted by the averaged simulations, providing for an overall taller flame.

When considering all $x/D$ planes (Supplementary material B), some common model disagreements are observed among the flames, such as a shallower-than-predicted temperature gradient and lower-than-predicted peak CO mole fractions in the reaction zones nearest the pilot ($x/D < 10$), and a lower-than-predicted core temperature in the highest plane measured ($x/D = 37.7$) for all fuels, suggesting some deficiencies in the turbulent mixing models. Additionally, the reaction zones (indicated by peak CO mole fraction) of the flames with heavier fuels ($n$-$C_7H_{16}$ and $C_6H_5CH_3$) are both experimentally observed at larger $r/D$ than predicted for $x/D < 10$, although the extent of the reaction zone for the flame fueled by the lighter $C_2H_4$ is well-predicted by the LES. The larger fuels $n$-$C_7H_{16}$ and $C_6H_5CH_3$ are both subject to heavy fuel pyrolysis [6,10,11], decomposing into fuel fragments whose diffusivities may not be as well-characterized as those produced by $C_2H_4$. As mixing of the pilot flow and hot co-flow with the reaction layer will have downstream influences [61], an underprediction of the mixing in the pilot region of the flame would have magnified fuel-specific effects on the downstream oxidation of fuels with sensitive low-temperature chemistry, such as $n$-heptane.

### 3.3. Thermochemical state-space analysis

An analysis of the thermochemical state-space representation of the experimental and numerical results is conducted by examining correlations between $X_{CO}$, $X_{CO_2}$ and temperature. Figure 11 compares instantaneous and averaged scatter data from the LES calculations of the three different flames with measurements. These scatter data are extracted along five axial planes for $x/D = \{2.5, 7.5, 15, 25, 35\}$. Where possible, $T$ determined from the $CO_2$ LAT measurements is used to map the experimental data for consistent comparison. The averaged scatter data shown are time-averaged in physical coordinates (similar to the time-averaging of the experimental data), which are subsequently mapped to the $X - T$ conditional space. We note that this is not necessarily equivalent to averaging the instantaneous data, and so regions of the flow with high variation will not necessarily produce averaged scatter data that lie within the instantaneous snapshots shown in Fig. 11. The instantaneous points nonetheless illustrate the predicted structure of the flame, while the averaged values are comparable to experimental data.

In general, it can be seen that major differences are confined to the upstream region of the flames that are represented by strong turbulence/chemistry coupling. For all fuels, the $x/D = 2.5$ plane is dominated by the $CO_2$ produced by the pilot flame as predicted by the LES, and both the predicted and experimentally observed CO state-spaces show similar behavior amongst the differ-
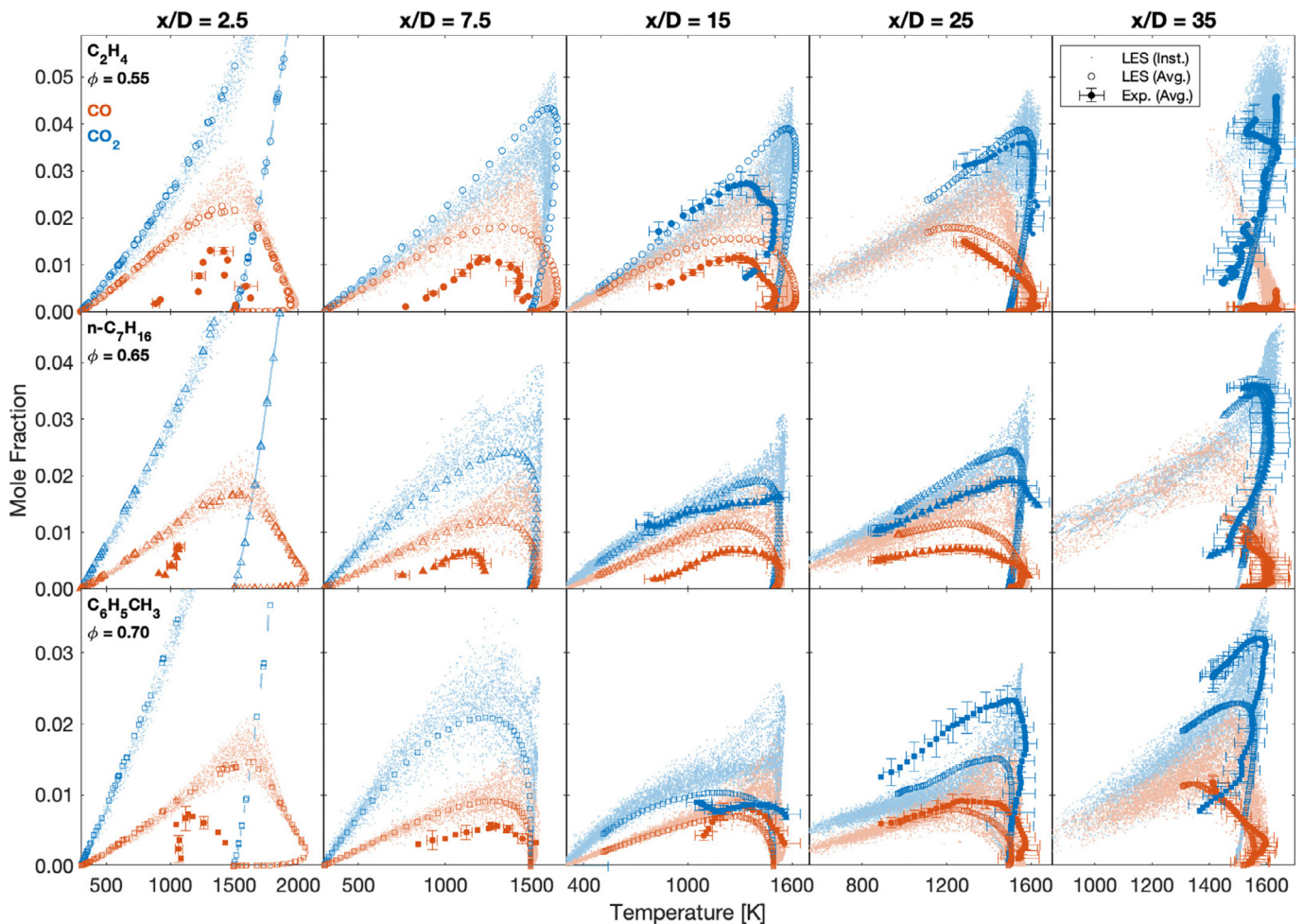
**Fig. 11.** Comparison of $X_{CO} - T$ and $X_{CO_2} - T$ correlation data at different axial locations for flames fueled by $C_2H_4$ (top row), $n$-$C_7H_{16}$ (middle row), and $C_6H_5CH_3$ (bottom row). Light-colored points indicate instantaneous LES data, open markers indicate time- and azimuthally-averaged LES data, and filled markers with error bars indicate experimental data. Some data points have been omitted for reader clarity.

ent fuels, with an overprediction of CO concentration in all cases. Slightly higher peak temperatures are predicted in the ($n$-$C_7H_{16}$)-air and ($C_6H_5CH_3$)-air flames, although this is less conclusive in the limited available experimental measurements in this plane. Fuel-specific effects become more apparent in the $x/D = 7.5$ plane, in which the ($C_2H_4$)-air flame shows higher predicted and measured temperatures and CO and $CO_2$ concentrations than the other flames. The thermochemical state-spaces of the ($n$-$C_7H_{16}$)-air and ($C_6H_5CH_3$)-air flames show a more diffuse distribution of temperatures than the ($C_2H_4$)-air flame, reflecting the increased sizes of the flame brushes in those flows.

The agreement between simulations and experiments improves with increasing downstream distance as the flame approaches thermochemical equilibrium. This is evident by the narrowing of the temperature scattering and the consumption of CO. Generally, $X_{CO}$ is overpredicted at lower values of $T$, and is in agreement within uncertainty at higher values of $T$. While averaged CO-mole fraction profiles are overpredicted for ($C_2H_4$)-air and ($C_6H_5CH_3$)-air flames, the opposite trend is observed for the normal alkane fuel. The $CO_2$ peak value increases for the large hydrocarbon fuels, showing the highest $CO_2$-emissions as a consequence of the overall stoichiometry. While predictions of $X_{CO} - T$ scatter for the ($C_2H_4$)-air and ($C_6H_5CH_3$)-air flames are in good agreement with experimental data throughout the flame, the CO formation is consistently overpredicted for the ($n$-$C_7H_{16}$)-air flame on the fuel-rich side, which we primarily attribute to discrepancies in the turbu-

lent mixing. Further measurements of the hydrodynamic flow-field are necessary to confirm this. The largest disagreements in thermochemical state-space exhibited by the fuel ($n$-$C_7H_{16}$) may also be partially attributed to a deficiency of the chemical model at low temperatures; since ignition delay was not a target parameter for the mechanism reduction efforts, low-temperature critical phenomena such as Negative Temperature Coefficient effects and low-temperature pyrolysis [6] are not captured by the models. The two-stage ignition behavior of $n$-$C_7H_{16}$ is appreciable below 800 K, suggesting that the oxidation in the cooler core of this premixed jet flame is significantly influenced by local chemical kinetic behavior relative to influence by mixing with the hot co-flow. Beyond the models in the current work, the overpredicted rates of oxidation in the premixed core of the ($n$-$C_7H_{16}$)-air flame observed in Figs. 4, 5, 10, and Supplementary material B are consistent with quantitative species time-histories ($CH_2O$, OH, $CO_2$, $H_2O$) measured in previous shock tube oxidation experiments [62], which demonstrated that the oxidation rates of $n$-$C_7H_{16}$ during low-temperature staged ignition are overpredicted by state-of-the-art chemical models.

## 4. Uncertainty analysis

In this paper, we report experimentally measured values of species concentration and temperature, but it is important to note the uncertainty in these values due to factors associated with the LAT measurement technique in turbulent flows. We follow the un-

certainty analysis presented in previous work [30], with added analysis in this work to account for uncertainty associated with tomographic reconstruction [32] and correlated fluctuations in the flowfield scalars associated with turbulent combustion [60].

### 4.1. Experimental measurement uncertainty

For Eqs. (1)–(3) as well as those in this section (unless otherwise noted), we follow the Taylor Series Method (TSM) of uncertainty propagation [63], in which the uncertainty of a variable $r$, $\Delta r$, is given by:

$$(\Delta r)^2 = \left(\frac{\partial r}{\partial x_1} \Delta x_1\right)^2 + \left(\frac{\partial r}{\partial x_2} \Delta x_2\right)^2 + \cdots \tag{8}$$

where $x_i$ are dependent variables and $\Delta x_i$ are their respective uncertainties. As indicated by Eq. 2, mole fraction of an absorbing species $X_{abs}(r)$ depends on linestrength $S_j(T(r))$ and reconstructed absorption coefficient $K_j(r)$. In turn, $S_j(T(r))$ depends on temperature $T(r)$, which—for the two-line thermometry techniques employed here—depends on $R(r)$, which is also dependent on $K_j(r)$. Here, we discuss the propagation of uncertainty from initial intensity measurements $I_t$ and $I_0$ through these equations to obtain uncertainty in $T(r)$ and $X_{abs}(r)$.

The systematic error in each $I_t$ and $I_0$ in Eq. (1) is assumed to be the same because the same system is used to measure both signals; thus the only uncertainty considered for each of these signals is the random uncertainty among all the scans averaged within a spatial segment $dr$ (in this case, the distance associated with 105 direct-absorption scans). For each spatial segment, the standard deviations of both the incident background $I_0$ and the absorbance signals $I_t$ are calculated, which are both used to determine the 95% confidence interval of the signals, represented by $\Delta I_0$ and $\Delta I_t$. To obtain the variation *specifically in absorbance*, $\Delta \alpha_\nu$, we subtract $\Delta I_0$ from $\Delta I_t$ and use the resulting value as a bounds on absorbance signal, $I_t \pm (\Delta I_t - \Delta I_0)$. We then calculate the resulting variation in $\alpha_\nu$, $\Delta \alpha_\nu$, by propagating the uncertainty in the Beer-Lambert law [48]. In turn, $\Delta A_{j,\text{proj}}(r)$ is calculated by propagating the uncertainty $\Delta \alpha_\nu$ in Eq. (1), generating an upper and lower bound on $A_{j,\text{proj}}(r)$. This process occurs for each spatial interval $dr$ across the radius of the flow $r$.

The experimental uncertainty of absorption coefficient, $\Delta K_j(r)$, comprises two primary sources and is calculated from:

$$(\Delta K_j(r))^2 = (\Delta K_{j,\Delta A_{j,\text{proj}}}(r))^2 + (\Delta K_{j,\Delta(r=0)}(r))^2 \tag{9}$$

$\Delta K_{j,\Delta A_{j,\text{proj}}}(r)$ is determined numerically via tomographic reconstruction of the upper and lower bounds of $A_{j,\text{proj}}(r)$. $\Delta K_{j,\Delta(r=0)}(r)$ is the uncertainty associated with the location of the centerline assumed in the Abel inversion ($r = 0.0 \pm 0.5$ mm), which more significantly affects the tomographic reconstruction in the core relative to the edges of the flow [32].

Applying Eq. (8) to the ratio of the two absorption coefficients $K_j(r)$, we can calculate the uncertainty in $R(r)$, $\Delta R(r)$:

$$\left(\frac{\Delta R(r)}{R(r)}\right)^2 = \left(\frac{\Delta K_A(r)}{K_A(r)}\right)^2 + \left(\frac{\Delta K_B(r)}{K_B(r)}\right)^2 \tag{10}$$

In the results presented in this study, the ratio $R(r)$ shown in Eq. (3) is used to determine temperature $T(r)$ by correlating $R(r)$ to simulations of $R(T) = S_A(T)/S_B(T)$ created using Eq. (13), which is shown later. Neglecting the influence of stimulated emission, an explicit expression revealing the uncertainty dependencies in temperature can be derived via the following analytical expression for temperature $T(r)$ [48]:

$$T(r) = \frac{\frac{hc}{k_B}\left(E_B'' - E_A''\right)}{\ln(R(r)) + \ln\left(\frac{S_B(T_0)}{S_A(T_0)}\right) + \frac{hc}{k_B}\frac{(E_B'' - E_A'')}{T_0}} \tag{11}$$

Here, $h$ [J·s] is the Planck constant, $c$ [cm/s] is the speed of light, $k_B$ [J/K] is the Boltzmann constant, and $E_j''$ [cm$^{-1}$] is the lower-state energy for the two lines $A$ and $B$. Since $T(r)$ is a function of $R(r)$, there is an associated uncertainty in temperature, $\Delta T(r)$. Using Eq. (8) on Eq. (11), $\Delta T(r)$ is given by:

$$\frac{\Delta T(r)^2}{T(r)^2} = \frac{(\Delta R(r)/R(r))^2}{\left(\ln(R(r)) + \ln\left(\frac{S_B(T_0)}{S_A(T_0)}\right) + \frac{hc}{k_B}\frac{(E_B'' - E_A'')}{T_0}\right)^2} \tag{12}$$

where $T_0$ is the linestrength reference temperature of 296 K [47]. When the mole fraction $X_{abs}(r)$ of the species approaches zero, both absorption coefficients $K_j(r)$ will also approach zero, and $R(r)$ will become highly sensitive to noise or error in either reconstruction of $K_j(r)$. This can lead to unreasonably high or low temperatures in regions where the signal-to-noise ratio of $K_j(r)$ is low (SNR < 5), and so we do not include those regions in the plots shown or in the dataset in Supplementary material B.

As mentioned, $S_j(T(r))$ is function of $T(r)$ [48]:

$$S_j(T) = S_j(T_0)\frac{Q(T_0)}{Q(T)}\frac{T_0}{T}\exp\left[-\frac{hcE_j''}{k_B}\left(\frac{1}{T} - \frac{1}{T_0}\right)\right]$$
$$\times \left[1 - \exp\left(-\frac{hc\nu_{0,j}}{k_BT}\right)\right]\left[1 - \exp\left(-\frac{hc\nu_{0,j}}{k_BT_0}\right)\right]^{-1} \tag{13}$$

where it is understood that $T$ is $T(r)$. $Q$ is the partition function for the internal energy modes of the molecule. Therefore, $\Delta T(r)$ (from the uncertainty in $\Delta R(r)$) affects $S_j(T(r))$ that is used to calculate mole fraction. The following expression can be obtained for the uncertainty in linestrength due to uncertainty in observed temperature, $\Delta T(r)$:

$$\Delta S_{j,T}^2(T) = S_j^2(T)\Delta T^2\left(-\frac{\partial Q(T)/\partial T}{Q(T)} - \frac{1}{T} + \frac{hcE_j''}{k_BT^2}\right.$$
$$\left. + \frac{hc\nu_{0,j}}{k_BT^2}\left(\frac{\exp\left(-hc\nu_{0,j}/k_BT\right)}{1 - \exp\left(-hc\nu_{0,j}/k_BT\right)}\right)\right)^2 \tag{14}$$

In practice, $\Delta S_{j,T}(T)$ is determined numerically from Eq. (13) via discrete differentiation with respect to $T$ according to Eq. (8). Additionally, the HITEMP database [47] reports uncertainty in the reference temperature linestrength $S_j(T_0)$ (2% for all spectral lines in this work), which we reference here as $\Delta S_j(T_0)$. Thus, the total uncertainty in linestrength can be calculated:

$$\Delta S_j^2(T) = \Delta S_{j,T}^2(T) + \Delta S_j^2(T_0) \tag{15}$$

Now, mole fraction is given by:

$$X_{abs}(r) = \frac{K_j(r)}{S_j(T(r))P} \tag{16}$$

Utilizing Eq. (8), the uncertainty in mole fraction, excluding uncertainty in total pressure $P$, is:

$$\left(\frac{\Delta X_{abs}(r)}{X_{abs}(r)}\right)^2 = \left(\frac{\Delta K_j(r)}{K_j(r)}\right)^2 + \left(\frac{\Delta S_j(T(r))}{S_j(T(r))}\right)^2 \tag{17}$$

Thus, the uncertainties in $\Delta K_j(r)$ and $\Delta S_j(T(r))$ are accounted for, and $\Delta T(r)$ and $\Delta X_{abs}(r)$ may be determined for all measurements.

### 4.2. The effect of correlated variables on measurements

Independent of the aforementioned uncertainties—which are readily quantifiable from the experimental data—we may also consider $\Delta K_{j,T'X'}$, the effect of correlated fluctuations of temperature and mole fraction [60] in the turbulent flowfield, from Eq. (6):

$$\Delta K_{j,T'X'} = aP\overline{T'X_{abs}'} = \left.\frac{\partial S_j(T)}{\partial T}\right|_{\overline{T}} \cdot P\overline{T'X_{abs}'} \tag{18}$$
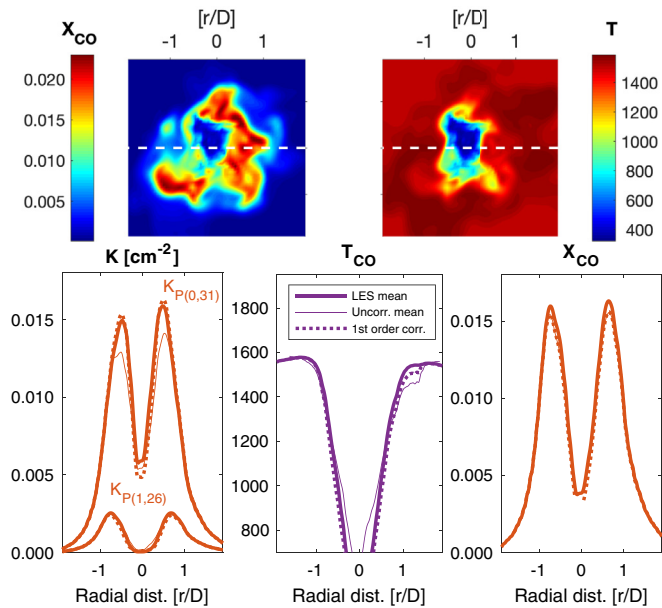
**Fig. 12.** *Top:* Instantaneous LES-predicted $X_{CO}$ and $T$ fields of the $(C_2H_4)$-air jet flame at $x/D = 15$. Correlation analysis line of sight marked by white dashed line. *Bottom:* Time-averaged $K_j$ (left), $T_{CO}$ (center), and $X_{CO}$ (right) from LES predictions. Values evaluated at $\overline{T}$ and $\overline{X}$ marked by thick lines, values determined from $\overline{K_j}$ marked by thin lines, and values determined from $\overline{K_j} + \Delta K_{j,T'X'}$ marked by dashed lines.

As mentioned previously, this simplified expression is obtained from a first-order Taylor expansion of the temperature-dependent linestrength $S_j(T) = aT + b$ in Eq. (2). In this expression, $a$ is the partial derivative of temperature-dependent linestrength with respect to temperature, $\partial S_j(T)/T|_{\overline{T}}$, and is evaluated numerically using Eq. (13) at the temperature determined through Eq. (3).

The effect of the correlated variables $T'X'_{abs}$ on $K_j(r)$ is estimated using temporally and spatially-resolved LES predictions of the jet flames for all fuels at the same $x/D$ planes as shown in Fig. 11. At each $x/D$ plane, the thermochemistry ($T$, $X_{CO}$, $X_{CO_2}$) predicted by LES at each radial location $r$ is used in a forward projection model [44] along a single line-of-sight to generate time-resolved profiles of $K_j(r)$. A representative instantaneous snapshot of the $X_{CO}$ and $T$ fields for the $(C_2H_4)$-air jet flame at $x/D = 15$ is shown in the top of Fig. 12. Time-averaged values of $K_j(r)$ with and without considering $\Delta K_{j,T'X'}$ are then used to calculate 'uncorrected' and 'first order corrected' $T(r)$ and $X_{abs}(r)$, respectively, and can be compared with the $K_j(r)$ values calculated from 'true mean' $T(r)$ and $X_{abs}(r)$ predicted by the LES. Representative estimates compared with the corresponding LES-predicted values of $T$ and $X_{CO}$ for the $x/D = 15$ plane of the $(C_2H_4)$-air jet flame over a 0.5 ms interval are shown in Fig. 12. In general, the first-order approximations of $\overline{K_j(r)}$ provided by $\Delta K_{j,T'X'}$ are in agreement with the $K_j(r)$ values calculated from 'true mean' LES thermochemistry, and some differences are observed between these values of $\overline{K_j(r)}$ and the 'uncorrected' values representing the measurement. The P(0,31) rovibrational transition of CO is more affected than the P(1,26) transition, likely owing to its behavior with temperature over the range of 300–1500 K [30]. The largest discrepancies are observed to be in the reaction zone and the core of the flame; these differences have a modest influence on temperature (maximum deviation of 100 K) and mole fraction (maximum relative deviation of 5%).

A representative summary of these influences as a function of $x/D$ for all fuels is provided in Fig. 13, in which the differences for predicted temperature and mole fraction at $r/D = 1$ (observed to be typically associated with the reaction zone) are plotted. Tem-
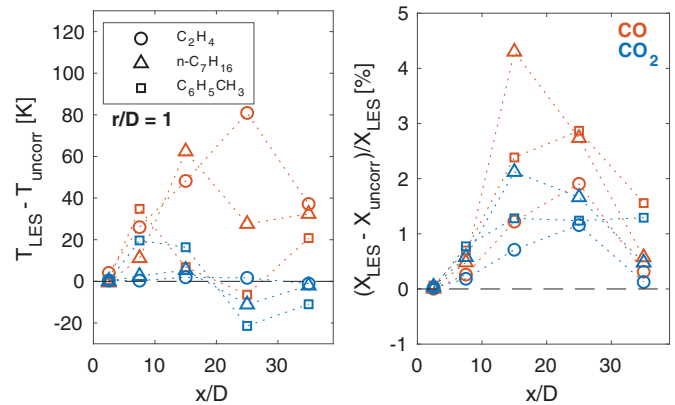


**Fig. 13.** Anticipated deviations in $T$ (left) and $X_{abs}$ (right) LAT measurements caused by correlated fluctuations of thermochemical scalars for each fuel at $r/D = 1$ as a function of $x/D$, estimated using time-resolved LES predictions over a 0.5 ms interval.

perature variations have been plotted as (True Value) - (Uncorrected Value), which may be readily added to the measurement data available in Supplementary material B, and the influence on mole fraction is plotted in terms of relative percentage for more direct comparison amongst fuels. The influence of the correlated variables $\overline{T'X'_{abs}}$ on temperature is predicted to be most significant at $x/D = 25$ for the $(C_2H_4)$-air jet flame, though the impact on relative mole fraction is most significant at $x/D = 15$ for the $(n\text{-}C_7H_{16})$-air jet flame. Overall, mole fraction and temperature determined from our LAT measurements of CO are more influenced by correlated fluctuations in flowfield scalars than those derived from our LAT measurements of $CO_2$. The influence is generally in the negative direction—therefore, values of temperature determined from time-averaged LAT measurements of these flows are expected to be nominally lower than the true mean more often than they are higher, and values of mole fraction are almost always expected to be lower.

Since these predicted influences of correlated variables on simulated $T$, $X_{CO}$, and $X_{CO_2}$ measurements are not based on experimental data, rather taken from LES results, and are within the reported experimental uncertainties, we do not attempt to correct the laser absorption tomography measurements shown in this paper. However, we note that this analysis is nonetheless relevant and useful for comparing the experimental measurements with both the LES predictions and experimental measurements of different flow conditions—in previous work [30], we found that temperatures determined from LAT measurements of CO at $x/D = 20.5$ for a $(C_2H_4)$-air jet flame were nominally lower than those determined from LAT measurements of $CO_2$ (This is also observed in the right of Fig. 7), and although the calculated temperatures agreed within experimental uncertainty, this nominal disagreement increased with increasing jet Reynolds number. Although more investigation is required to confirm that this was caused by the influence of correlated fluctuations on the time-averaged measurements, the preceding analysis may provide an explanation. This influence of correlated variables in turbulent flows may be mitigated in future LAT measurements on PPJB-type flames through transition selection. We further note that point measurements providing experimental data on the scalar fluctuations may be complimentary to the current LAT method and help refine flow-field characterization.

## 5. Conclusions

In this study, quantitative spatially-resolved profiles of carbon monoxide, carbon dioxide, and temperature were obtained

via mid-infrared laser absorption tomography in turbulent premixed jet flames of different fuels (ethylene, n-heptane, and toluene). The chosen fuels encompass a diverse sample of molecular structures encountered in practical energy conversion devices: alkenes, normal alkanes, and aromatics. The novel dataset of 2D thermochemical measurements—which defines a heat release boundary associated with the kinetically-slow CO to $CO_2$ conversion—was directly compared with results of turbulent combustion simulations using LES methods. Fuel-specific effects are noted in both the multi-dimensional measurements and the modeling results; specifically, wider and taller flame brushes for the heavier molecular weight fuels are observed, indicating larger overall reaction zones for these flames despite normalization by flame speed. The LES predictions for all flames show generally good quantitative agreement with measurements, with larger discrepancies observed in upstream regions of the flames for the larger-molecular-weight fuels examined, namely *n*-heptane and toluene. A thermochemical state-space analysis was conducted, revealing potential discrepancies in the turbulent mixing and residual deficiencies in the low-temperature chemical model, representing opportunities for further investigation and model refinement.

The present study represents a distinct diagnostic advancement beyond prior investigative efforts on the Piloted Premixed Jet Burner, enabling direct quantitative comparison of absolute mole fraction measurements in two dimensions with predictions by state-of-the-art large eddy simulations and providing more granular and well-defined heat-release constraints for these models than the qualitative scalar intensity measurements from chemiluminescence. Moreover, our use of the large eddy simulation results to predict the influence of turbulent combustion scalar correlations on time-averaged experimental measurements highlights the enhanced value of a coupled numerical and experimental approach. Opportunities for further investigations and enhancements have been identified through combined measurement techniques. More broadly, the coupled experimental and numerical investigation, united by quantitative thermochemical scalars, demonstrates a uniquely powerful approach to advance turbulent combustion models and diagnostics for a wide range of fuels, experimental configurations, and operating conditions.

## Declaration of Competing Interest

The authors declare that they have no known competing financial interests or personal relationships that could have appeared to influence the work reported in this paper.

## Acknowledgments

## Supplementary material

Supplementary material associated with this article can be found, in the online version, at doi:10.1016/j.combustflame.2020.08.008

## References

[1] J.F. Driscoll, Turbulent premixed combustion: flamelet structure and its effect on turbulent burning velocities, Progr. Energy Combust. Sci. 34 (1) (2008) 91–134, doi:10.1016/j.pecs.2007.04.002.

[2] A.N. Lipatnikov, J. Chomiak, Effects of premixed flames on turbulence and turbulent scalar transport, Progr. Energy Combust. Sci. 36 (1) (2010) 1–102, doi:10.1016/j.pecs.2009.07.001.

[3] S.G. Davis, C.K. Law, Determination of and fuel structure effects on laminar flame speeds of C1 to C8 hydrocarbons, Combust. Sci. Technol. 140 (1–6) (1998) 427–449, doi:10.1080/00102209808915781.

[4] Z. Zhao, J. Li, A. Kazakov, F. Dryer, S. Zeppieri, Burning velocities and a high-temperature skeletal kinetic model for n-decane, Combust. Sci. Technol. 177 (2004) 89–106, doi:10.1080/00102200590883769.

[5] K. Kumar, C.J. Sung, Laminar flame speeds and extinction limits of preheated n-decane/O2/N2 and n-dodecane/O2/N2 mixtures, Combust. Flame 151 (1–2) (2007) 209–224, doi:10.1016/j.combustflame.2007.05.002.

[6] H. Wang, R. Xu, K. Wang, C.T. Bowman, R.K. Hanson, D.F. Davidson, K. Brezinsky, F.N. Egolfopoulos, A physics-based approach to modeling real-fuel combustion chemistry - I. Evidence from experiments, and thermodynamic, chemical kinetic and statistical considerations, Combust. Flame 193 (2018) 502–519, doi:10.1016/J.COMBUSTFLAME.2018.03.019.

[7] F. Dinkelacker, A. Soika, D. Most, D. Hofmann, A. Leipertz, W. Polifke, K. Döbbeling, Structure of locally quenched highly turbulent lean premixed flames, Sympos. (Int.) Combust. 27 (1) (1998) 857–865, doi:10.1016/S0082-0784(98)80482-7.

[8] A.Y. Poludnenko, E.S. Oran, The interaction of high-speed turbulence with flames: Global properties and internal flame structure, Combust. Flame 157 (5) (2010) 995–1011, doi:10.1016/j.combustflame.2009.11.018.

[9] C. Ji, E. Dames, B. Sirjean, H. Wang, F.N. Egolfopoulos, An experimental and modeling study of the propagation of cyclohexane and mono-alkylated cyclohexane flames, Proc. Combust. Inst. 33 (1) (2011) 971–978, doi:10.1016/j.proci.2010.06.099.

[10] J. Smolke, F. Carbone, F.N. Egolfopoulos, H. Wang, Effect of n-dodecane decomposition on its fundamental flame properties, Combust. Flame 190 (2018) 65–73, doi:10.1016/j.combustflame.2017.11.009.

[11] A. Holley, X. You, E. Dames, H. Wang, F. Egolfopoulos, Sensitivity of propagation and extinction of large hydrocarbon flames to fuel diffusion, Proc. Combust. Inst. 32 (2009) 1157–1163, doi:10.1016/j.proci.2008.05.067.

[12] A.N. Lipatnikov, J. Chomiak, Molecular transport effects on turbulent flame propagation and structure, Progr. Energy Combust. Sci. 31 (1) (2005) 1–73, doi:10.1016/j.pecs.2004.07.001.

[13] T.M. Wabel, A.W. Skiba, J.E. Temme, J.F. Driscoll, Measurements to determine the regimes of premixed flames in extreme turbulence, Proc. Combust. Inst. 36 (2) (2017) 1809–1816, doi:10.1016/j.proci.2016.08.065.

[14] M.J. Dunn, A.R. Masri, R.W. Bilger, A new piloted premixed jet burner to study strong finite-rate chemistry effects, Combust. Flame 151 (1–2) (2007) 46–60, doi:10.1016/j.combustflame.2007.05.010.

[15] M.J. Dunn, A.R. Masri, R.W. Bilger, R.S. Barlow, Finite rate chemistry effects in highly sheared turbulent premixed flames, Flow Turb. Combust. 85 (3–4) (2010) 621–648.

[16] F. Carbone, J.L. Smolke, A.M. Fincham, F.N. Egolfopoulos, Comparative behavior of piloted turbulent premixed jet flames of C1–C8 hydrocarbons, Combust. Flame 180 (2017) 88–101, doi:10.1016/j.combustflame.2017.02.030.

[17] L. Paxton, A. Giusti, E. Mastorakos, F.N. Egolfopoulos, Assessment of experimental observables for local extinction through unsteady laminar flame calculations, Combust. Flame 207 (2019) 196–204, doi:10.1016/j.combustflame.2019.05.043.

[18] J. Smolke, S. Lapointe, L. Paxton, G. Blanquart, F. Carbone, A.M. Fincham, F.N. Egolfopoulos, Experimental and numerical studies of fuel and hydrodynamic effects on piloted turbulent premixed jet flames, Proc. Combust. Inst. 36 (2) (2017) 1877–1884, doi:10.1016/j.proci.2016.07.127.

[19] L. Paxton, J. Smolke, F.N. Egolfopoulos, Effects of heat release and fuel type on highly turbulent premixed jet flames, Proc. Combust. Inst. 37 (2) (2019) 2565–2572, doi:10.1016/j.proci.2018.08.041.

[20] M.J. Dunn, A.R. Masri, R.W. Bilger, R.S. Barlow, G.H. Wang, The compositional structure of highly turbulent piloted premixed flames issuing into a hot coflow, Proc. Combust. Inst. 32 (2) (2009) 1779–1786, doi:10.1016/j.proci.2008.08.007.

[21] F. Fuest, R.S. Barlow, G. Magnotti, J.A. Sutton, Scalar dissipation rates in a turbulent partially-premixed dimethyl ether/air jet flame, Combust. Flame 188 (2018) 41–65, doi:10.1016/j.combustflame.2017.09.020.

[22] T.A. McManus, I.T. Monje, J.A. Sutton, Experimental assessment of the Tenti S6 model for combustion-relevant gases and filtered Rayleigh scattering applications, Appl. Phys. B 125 (1) (2019) 1–23, doi:10.1007/s00340-018-7121-8.

[23] V. Bergmann, W. Meier, D. Wolff, W. Stricker, Application of spontaneous Raman and Rayleigh scattering and 2D LIF for the characterization of a turbulent CH4/H2/N2 jet diffusion flame, Appl. Phys. B 66 (4) (1998) 489–502, doi:10.1007/s003400050424.

[24] R. Cabra, J.Y. Chen, R.W. Dibble, A.N. Karpetis, R.S. Barlow, Lifted methane-air jet flames in a vitiated coflow, Combust. Flame 143 (4) (2005) 491–506, doi:10.1016/j.combustflame.2005.08.019.

[25] M.J. Dunn, A.R. Masri, R.W. Bilger, R.S. Barlow, Finite rate chemistry effects in highly sheared turbulent premixed flames, Flow Turbul. Combust. 85 (3–4) (2010) 621–648, doi:10.1007/s10494-010-9280-5.

[26] B.R. Halls, J.R. Gord, T.R. Meyer, D.J. Thul, M. Slipchenko, S. Roy, 20-kHz-rate three-dimensional tomographic imaging of the concentration field in a turbulent jet, Proc. Combust. Inst. 36 (3) (2017) 4611–4618, doi:10.1016/j.proci.2016.07.007.

[27] R.S. Barlow, G.J. Fiechtner, C.D. Carter, J.Y. Chen, Experiments on the scalar structure of turbulent CO/H2/N2 jet flames, Combust. Flame 120 (4) (2000) 549–569, doi:10.1016/S0010-2180(99)00126-1.

[28] C.S. Goldenstein, R.M. Spearrin, J.B. Jeffries, R.K. Hanson, Infrared laser-absorption sensing for combustion gases, Progr. Energy Combust. Sci. 60 (2017) 132–176, doi:10.1016/j.pecs.2016.12.002.

[29] W. Cai, C.F. Kaminski, Tomographic absorption spectroscopy for the study of gas dynamics and reactive flows, Progr. Energy Combust. Sci. 59 (2017) 1–31, doi:10.1016/j.pecs.2016.11.002.

[30] C. Wei, D.I. Pineda, L. Paxton, F.N. Egolfopoulos, R.M. Spearrin, Mid-infrared laser absorption tomography for quantitative 2D thermochemistry measurements in premixed jet flames, Appl. Phys. B 124 (6) (2018) 123, doi:10.1007/s00340-018-6984-z.

[31] C.J. Dasch, One-dimensional tomography: a comparison of Abel, onion-peeling, and filtered backprojection methods, Appl. Opt. 31 (8) (1992) 1146, doi:10.1364/AO.31.001146.

[32] K.J. Daun, K.A. Thomson, F. Liu, G.J. Smallwood, Deconvolution of axisymmetric flame properties using Tikhonov regularization, Appl. Opt. 45 (19) (2006) 4638, doi:10.1364/AO.45.004638.

[33] R.S. Barlow, J.H. Frank, A.N. Karpetis, J.Y. Chen, Piloted methane/air jet flames: transport effects and aspects of scalar structure, Combust. Flame 143 (4) (2005) 433–449, doi:10.1016/j.combustflame.2005.08.017.

[34] Y. Chen, M. Ihme, Large-eddy simulation of a piloted premixed jet burner, Combust. Flame 160 (12) (2013) 2896–2910, doi:10.1016/j.combustflame.2013.07.009.

[35] F. Grøvdal, S. Sannan, J.Y. Chen, A.R. Kerstein, T. Løvås, Three-dimensional linear eddy modeling of a turbulent lifted hydrogen jet flame in a vitiated co-flow, Flow Turbul. Combust. 101 (4) (2018) 993–1007, doi:10.1007/s10494-018-9963-x.

[36] R.J. Kee, J. Miller, M.D. Smooke, J.F. Grcar, PREMIX: a Fortran program for modeling steady laminar one-dimensional premixed flames, Technical Report, Sandia National Laboratories, Livermore, CA, USA, 1985.

[37] R. Villarreal, P.L. Varghese, Frequency-resolved absorption tomography with tunable diode lasers, Appl. Opt. 44 (31) (2005) 6786–6795, doi:10.1364/AO.44.006786.

[38] P. Nau, J. Koppmann, A. Lackner, K. Kohse-Höinghaus, A. Brockhinke, Quantum cascade laser-based MIR spectrometer for the determination of CO and CO2 concentrations and temperature in flames, Appl. Phys. B 118 (3) (2015) 361–368, doi:10.1007/s00340-014-5992-x.

[39] X. Liu, G. Zhang, Y. Huang, Y. Wang, F. Qi, Two-dimensional temperature and carbon dioxide concentration profiles in atmospheric laminar diffusion flames measured by mid-infrared direct absorption spectroscopy at 4.2 $\mu$m, Appl. Phys. B 124 (4) (2018) 61, doi:10.1007/s00340-018-6930-0.

[40] X. Liu, G. Wang, J. Zheng, L. Xu, S. Wang, L. Li, F. Qi, Temporally resolved two dimensional temperature field of acoustically excited swirling flames measured by mid-infrared direct absorption spectroscopy, Opt. Express 26 (24) (2018) 31983, doi:10.1364/oe.26.031983.

[41] C. Wei, D.I. Pineda, C.S. Goldenstein, R.M. Spearrin, Tomographic laser absorption imaging of combustion species and temperature in the mid-wave infrared, Opt. Express 26 (16) (2018) 20944, doi:10.1364/OE.26.020944.

[42] R.J. Tancin, R.M. Spearrin, C.S. Goldenstein, 2D mid-infrared laser-absorption imaging for tomographic reconstruction of temperature and carbon monoxide in laminar flames, Opt. Express 27 (10) (2019) 14184, doi:10.1364/OE.27.014184.

[43] D.I. Pineda, J.L. Urban, R.M. Spearrin, Interband cascade laser absorption of hydrogen chloride for high-temperature thermochemical analysis of fire-resistant polymer reactivity, Appl. Opt. 59 (7) (2020) 2141, doi:10.1364/AO.386536.

[44] C. Wei, K.K. Schwarm, D.I. Pineda, R.M. Spearrin, Deep neural network inversion for 3D laser absorption imaging of methane in reacting flows, Opt. Lett. 45 (8) (2020) 2447–2450, doi:10.1364/ol.391834.

[45] F.A. Bendana, I.C. Sanders, J.J. Castillo, C.G. Hagström, D.I. Pineda, R.M. Spearrin, In-situ thermochemical analysis of hybrid rocket fuel oxidation via laser absorption tomography of CO, CO2, and H2O, Exp. Fluids 61 (190) (2020), doi:10.1007/s00348-020-03004-7.

[46] S. Gazzola, P.C. Hansen, J.G. Nagy, IR Tools: a MATLAB package of iterative regularization methods and large-scale test problems, Numer. Algor. 81 (3) (2019) 773–811, doi:10.1007/s11075-018-0570-7.

[47] L. Rothman, I. Gordon, R. Barber, H. Dothe, R. Gamache, A. Goldman, V. Perevalov, S. Tashkun, J. Tennyson, HITEMP, the high-temperature molecular spectroscopic database, J. Quant. Spectrosc. Radiat. Transf. 111 (15) (2010) 2139–2150, doi:10.1016/j.jqsrt.2010.05.001.

[48] R.K. Hanson, R.M. Spearrin, C.S. Goldenstein, Spectroscopy and Optical Diagnostics for Gases, Springer International Publishing, Cham, 2016, doi:10.1007/978-3-319-23252-2.

[49] O. Colin, F. Ducros, D. Veynante, T. Poinsot, A thickened flame model for large eddy simulations of turbulent premixed combustion, Phys. Fluids 12 (7) (2000) 1843–1863, doi:10.1063/1.870436.

[50] A. Vreman, An eddy-viscosity subgrid-scale model for turbulent shear flow: algebraic theory and applications, Phys. Fluids 16 (10) (2004) 3670–3681, doi:10.1063/1.1785131.

[51] Y. Khalighi, F. Ham, J. Nichols, S.K. Lele, P. Moin, Unstructured large eddy simulation for prediction of noise issued from turbulent jets in various configurations, 17th AIAA/CEAS Aeroacoustics Conference (32nd AIAA Aeroacoustics Conference) (2011), p. 2886, doi:10.2514/6.2011-2886.

[52] P.C. Ma, Y. Lv, M. Ihme, An entropy-stable hybrid scheme for simulations of transcritical real-fluid flows, J. Comput. Phys. 340 (2017) 330–357.

[53] G. Strang, On the construction and comparison of difference schemes, SIAM J. Num. Anal. 5 (3) (1968) 506–517.

[54] S. Gottlieb, C.-W. Shu, E. Tadmor, Strong stability-preserving high-order time discretization methods, SIAM Rev. 43 (1) (2001) 89–112, doi:10.1137/S003614450036757X.

[55] H. Wu, P.C. Ma, M. Ihme, Efficient time-stepping techniques for simulating turbulent reactive flows with stiff chemistry, Comput. Phys. Commun. 243 (2019) 81–96.

[56] T. Lu, C.K. Law, A directed relation graph method for mechanism reduction, Proc. Combust. Inst. 30 (1) (2005) 1333–1341, doi:10.1016/j.proci.2004.08.145.

[57] D.G. Goodwin, R.L. Speth, H.K. Moffat, B.W. Weber, Cantera: an object-oriented software toolkit for chemical kinetics, thermodynamics, and transport processes, 2018, (https://www.cantera.org). Version 2.4.0. 10.5281/zenodo.1174508.

[58] H. Wang, X. You, A.V. Joshi, S.G. Davis, others, USC Mech Version II. High-Temperature Combustion Reaction Model of H2/CO/C1-C4 Compounds, 2007.

[59] H. Wang, E. Dames, B. Sirjean, D.A. Sheen, R. Tango, A. Violi, J.Y.W. Lai, F.N. Egolfopoulos, D.F. Davidson, R.K. Hanson, C.T. Bowman, C.K. Law, W. Tsang, N.P. Cernansky, D.L. Miller, R.P. Lindstedt, A high-temperature chemical kinetic model of n-alkane (up to n-dodecane), cyclohexane, and methyl-, ethyl-, n-propyl and n-butyl-cyclohexane oxidation at high temperatures, JetSurF version 2.0, 2010.

[60] H. Tennekes, J.L. Lumley, A First Course in Turbulence, The MIT Press, Cambridge, MA, 1972.

[61] H. Wang, E.R. Hawkes, B. Savard, J.H. Chen, Direct numerical simulation of a high Ka CH4/air stratified premixed jet flame, Combust. Flame 193 (2018) 229–245, doi:10.1016/j.combustflame.2018.03.025.

[62] M.F. Campbell, S. Wang, C.S. Goldenstein, R.M. Spearrin, A.M. Tulgestke, L.T. Zaczek, D.F. Davidson, R.K. Hanson, Constrained reaction volume shock tube study of n-heptane oxidation: ignition delay times and time-histories of multiple species and temperature, Proc. Combust. Inst. 35 (1) (2015) 231–239, doi:10.1016/j.proci.2014.05.001.

[63] H.W. Coleman, W.G. Steele, Experimentation, Validation, and Uncertainty Analysis for Engineers, 3rd, John Wiley & Sons, Inc., Hoboken, NJ, USA, 2009.